

# Hyperspectral imaging acquisition set-up for medical applications

Marco La Salvia<sup>\*a</sup>, Emanuele Torti<sup>a</sup>, Giacomo Lago<sup>a</sup>, Raquel Leon<sup>b</sup>, Roberto Gandolfi<sup>a</sup>, Giulia Silveri<sup>c</sup>, Massimo Rossella<sup>d</sup>, Giovanni Danese<sup>a</sup>; Paolo Lago<sup>c</sup>, Francesco Loporati<sup>a</sup>

<sup>a</sup>Dept. of Electrical, Computer and Biomedical Engineering, University of Pavia, Pavia, Italy, IT27100; <sup>b</sup>Institute for Applied Microelectronics (IUMA), University of Las Palmas de Gran Canaria, Las Palmas de Gran Canaria, Spain, E35017; <sup>c</sup>Fondazione IRCCS Policlinico San Matteo, Pavia, Italy, IT27100; <sup>d</sup>Dept. of Physics, University of Pavia, Pavia, Italy, IT27100;

## ABSTRACT

Hyperspectral imaging (HSI) is a promising practice in research medicine due to its non-contact, non-invasive, non-ionizing, and label-free characteristics. Chromophores, such as haemoglobin and melanin, are responsible for the chemical structure of tissues and determine their spectral properties. Therefore, hyperspectral technologies might serve the role of tissue diagnosis, aiding physicians during surgical or clinical operations. Hence, hyperspectral cameras produce the data used by machine and deep learning algorithms to discriminate healthy from damaged tissues. Nevertheless, data quality remains an issue, especially concerning the small-sized medical dataset available to research. Here, we propose a hyperspectral imaging blueprint, designed to work with pushbroom sensors, representing one of the highest quality transducers to acquire spectral data. Indeed, pushbroom sensors only seize one scene line at a time, offering high spatial and spectral resolutions. It can work in any scenario, such as dermatological or surgical, involving a motionless subject. We designed the system to be affordable, open-source and robust. Therefore, it comprises Python libraries, an Arduino one board, a Nema17 stepper motor, its driver controller, and a recirculating ball screw for accurate movement. Furthermore, it offers a diode-based targeting system, attached to a 3D printed circular crown and built to hit the image capture and measure the right focusing distance. We equipped the blueprint with a graphical user interface to let physicians interact with the camera, accurately move it, and acquire the diagnostic data needed.

**Keywords:** Hyperspectral imaging, skin cancer, computer-aided diagnosis, medicine, bioengineering

## 1. INTRODUCTION

Skin tumour affects the most significant body organ, thus being one of the most frequent malignancies<sup>1</sup>, it originates in the epidermis and can affect three cell types: squamous, basal or melanocytes. Healthcare providers cluster epidermal lesions into melanoma and non-melanoma skin cancer (MSC - NMSC). The MSC initiates from any cell that produces melanin and comprises three subtypes: superficial extension, lentigo maligna, and nodular<sup>2</sup>. Most skin cancers retain genetic mutations that grow and spread over the body if left untreated, yielding potentially metastasising conditions.

Even though MSC is the rarest epidermal lesion, it is the most lethal as it lacks sufficient early detection. NMSC lesions represent more than 98% of skin lesions in the United States of America: 75–80% are basal cell carcinoma (BCC), 15–20% are squamous cell carcinoma (SCC), and around 1.6% are MSC<sup>3</sup>. Doctors must consider BCC and SCC malignant as they might induce death<sup>4</sup>. Consequently, arranging epidermal tumours into benign and malignant classes is more accurate. Nowadays, a person has a 4% chance of contracting melanoma, accounting for 75% of all skin cancer-related deaths<sup>3,5–7</sup>.

Dermatologists visually examine melanocytic lesions to determine the presence of malignancies during daily clinical practice, operating a handheld instrument having magnifying lenses and uniform polarised illumination. The procedure leans upon the so-called ABCDE rule, where A stands for asymmetry, B for border irregularity, C for colour, D for diameter, and E for evolution<sup>7</sup>. Nevertheless, this procedure causes benign lesions classified as malignant, thus introducing false positives. Consequently, the gold standard consists of a surgical lesion excision and histopathological evaluation<sup>7,8</sup>. This process is painful, time-consuming, slow, and expensive<sup>5</sup>. Undoubtedly, skin cancer incidence keeps escalating, carrying heavy health and economic responsibility for diagnosis and treatment. Early skin cancer detection effectively improves the 5-year survival rate and is correlated with 99% of the overall healing chances. Therefore, the escalating rate of skin cancers and the lack of adequate expertise and innovative methodologies present an immediate demand for systems based on artificial intelligence (AI) and novel optical technologies to assist clinicians in this domain<sup>7,9,10</sup>.

Hyperspectral imaging (HSI) is a non-invasive, non-ionising, and label-free procedure, initially designed for remote-sensing intentions, being researched in medicine for cancer detection thanks to recent technical refinements<sup>7,11</sup>. Hyperspectral (HS) images measure the reflected or transmitted light, collecting light-matter interaction values associated with several wavelengths of the electromagnetic spectrum range with low to high spatial resolution. HS images, also called *hypercubes*, form by aligning multiple 2D images in adjacent narrow wavelengths, yielding a reflectance spectrum of all the pixels<sup>11-13</sup>. Thus, the HS cube contains spatial and spectral information from the sample under analysis.

Chromophores, such as melanin and haemoglobin, are organic molecules that characterise epidermal lesions' spectral properties and vary among skin lesions of diverse etiologies. Consequently, HSI systems should capture such information, enabling machine learning (ML) algorithms to automatically detect and cluster tumours of various categories<sup>7,12,14</sup>. The visible light spectrum restricts conventional imaging strategies, leading to limited diagnosis. However, HS images set the stage for broadband information acquisition, overcoming the inter-class similarities and intra-class dissimilarities of the diseases that are hardly noticeable in the visual domain<sup>9,11,12</sup>.

Hyperspectral imaging uses a spectrometer, an instrument that measures the electromagnetic field, to collect spectral information, and this device is called a *hyperspectral camera*. These cameras collect information concerning hundreds of spectral bands with continuity over the entire spectrum of interest. Various acquisition techniques exist to obtain a hyperspectral image<sup>15</sup>. The most used are *whiskbroom*, *pushbroom*, *staring* and *snapshot*.

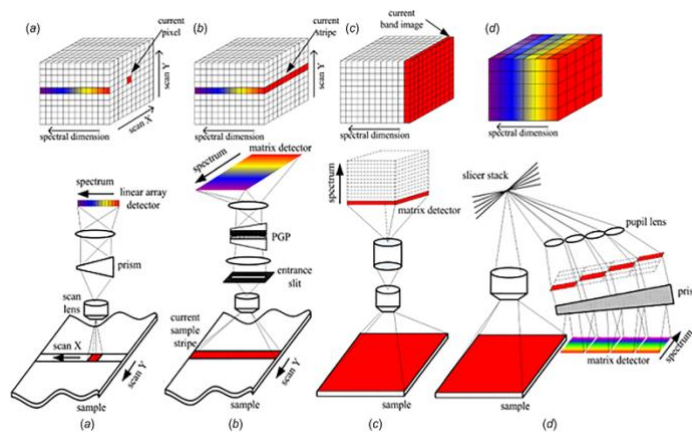


Figure 1 - Typical spectral imaging approaches. (a) Whiskbroom. (b) Pushbroom. (c) Staring. (d) Snapshot<sup>15</sup>

Figure 1 shows that the whiskbroom mode builds the *hypercube* ( $X, Y, \lambda$ ) by imaging the scene in the  $X$  and  $Y$  dimensions while collecting the wavelength domain ( $\lambda$ ). Since it involves separate image acquisition along the two spatial dimensions, it requires a complex hardware configuration and a high scanning time. The second procedure, also known as *pushbroom*, allows the grouping of no longer a single point but a line, with one spatial and one spectral dimension at a time. Figure 1 describes the 3D data cube formation upon sample movement: the relative movement must be synchronous with the acquisition rate of the detector frames to produce a uniform image. A *Pushbroom* scanner fetches more light than a whiskbroom, owing to its extended exposure, hence higher spectral resolution. The *staring* mode uses a filtered detector matrix to gather a single-band 2D grayscale image with spatial information  $X$  and  $Y$  at once. After passing through focusing optics, the filter splits light to collect a small narrow band segment of the spectrum at a time. Figure 1 displays the hypercube originated from defining the filter's wavelength as a function of time. Finally, the *snapshot* mode allows spatial and spectral information recording with a single exposure without scanning. The advantage is acquiring the entire scene in a single shot regarding spectral and spatial resolution. Regardless, snapshot cameras retain low spatial and spectral resolution.

Hyperspectral cameras also feature different hardware, which characterises wavelength sensitivity. Literature divides HS cameras into:

- VNIR (Visible Near Infrared): wavelengths from 400 nm to 1000 nm

- NIR (Near Infrared): wavelengths from 900 nm to 1700 nm
- SWIR (Short Wave Infrared): wavelengths from 1000 nm to 2500 nm
- LWIR (Long Wave Infrared): wavelengths from 8000 nm to 12000 nm

Concerning healthcare applications, academics have designed hyperspectral image acquisition systems concerning skin, brain, and plastic samples<sup>14,16,17</sup>. Nonetheless, these studies present drawbacks such as camera type, sensor fusion complexity or real-world scenario applicability. Present solutions differ mainly in the camera employed, their cost and weight, the materials used and the presence of customised graphical user interfaces (GUIs). The first employs a snapshot camera to image the region of interest, offering the lowest spatial and spectral resolution among the cameras. The second comprises two pushbroom cameras to offer different wavelength sensitivity, thus offering higher spatio-spectral resolution but high processing times, sensor fusion synchronisation and device weight-critical issues. Finally, although the latter comprises pushbroom cameras for plastic analysis discussing their laboratory implementation, it presents high-cost and implementation challenges.

Here, we present research to overcome the challenges mentioned above, introducing a hyperspectral imaging blueprint designed to work with pushbroom sensors, one of the highest-quality detectors, to image a region of interest. It works in various contexts, and we conceived it for either dermatological or surgical procedures which involve a motionless subject. We designed the system to be inexpensive, open-source and consistent. Accordingly, it includes Python libraries, an Arduino one board, a Nema17 stepper motor, its driver controller, and a recirculating ball screw for accurate movement. Likewise, it offers a diode-based targeting system, hooked to a 3D-printed circular crown, and built to measure the right focusing distance. We provided the blueprint with a GUI to let healthcare professionals interact with the imaging system, move it with high precision, and gather the diagnostic data needed.

In conclusion, the main contribution of our work is the proposal of an affordable hyperspectral imaging system, together with its detailed implementation description. Furthermore, not only do we discuss its development challenges and strategies, providing a GUI to automatically initiate the calibration and acquisition protocols and subsequent data storage, but also its validation approaches to allow work reproducibility.

## 2. ACQUISITION SET-UP AND BUILDING BLOCKS

The acquisition system created in this manuscript includes a hyperspectral camera, a movement system consisting of a linear ball screw guide, a stepping motor and a driver connected to an Arduino Uno board. Light sources also allow adequate illumination of the target in the spectrum of interest. One of the designed system's main objectives is automatically imaging skin areas with pushbroom sensors with few adaptations. The only step needed is a black and a white reference image acquisition for subsequent calibration preprocessing.

This section provides all the information concerning the system's design and building blocks in terms of hardware and software modules. Figure 2 displays the hyperspectral imaging platform system.



Figure 2 - Hyperspectral imaging system presented blueprint

## 2.1 Specim FX-10e hyperspectral camera

The system designed in this manuscript operates with pushbroom cameras that can acquire only one strip of pixels at a time<sup>15</sup>. They require the movement of the target object or the camera to scan the entire scene. The camera used in this study is a Specim FX10e, and it is a VNIR camera, therefore sensitive to visible and near-infrared wavelengths between 400 nm and 1000 nm.

Table I shows some relevant technical characteristics of the FX10e model. Table II instead describes the optical characteristics provided by the manufacturer's datasheet. The camera's lens has a 1.7 F-number, which is the ratio between the focal distance  $f$  and the diameter of the lens. The Field Of View (FOV), the detector's sensitivity angle to electromagnetic radiation, is  $38^\circ$ , and we operated a 15 cm focusing distance.

Table I - Specim FX10e hyperspectral camera specifications

TECHNICAL SPECIFICATIONS	FX10E
SPECTRAL RANGE	<b>400-1000 nm</b>
DETECTOR TYPE	<b>CMOS</b>
SLIT WIDTH	<b>Physical width 42 <math>\mu\text{m}</math>. Projection on sensor 32 <math>\mu\text{m}</math>.</b>
PIXEL PITCH	<b>16x8 <math>\mu\text{m}</math></b>
# SPATIAL PIXELS	<b>1024</b>
BINNING (SPECTRAL X SPATIAL)	<b>2 x 1</b>
SPECTRAL BINNING OPTIONS	<b>2x   4x   8x</b>
# SPECTRAL BANDS COVERING THE SPECIFIED RANGE	<b>224   112   56</b>
SPECTRAL SAMPLING/PIXEL	<b>2.7 nm   5.4 nm   10.8 nm</b>
SPECTRAL RESOLUTION FWHM	<b>5.5 nm (mean)</b>
SNR	<b>600:1</b>
FRAME RATE (FPS) FULL RANGE (220BANDS) MAX	<b>330 fps</b>
FRAME RATE (FPS) MROI EXAMPLES	<b>20 bands = 2800 fps 5 bands = 6500 fps</b>
SHUTTER	<b>Electromechanical shutter for dark background registration</b>

Table II - Specim FX10e optical characteristics

OPTICAL SPECIFICATIONS	FX10E
SPECTRAL RANGE	400 -1000 nm
F NUMBER	1.7
FOV	38°
FOCUSING DISTANCE	150 mm

The *pixel pitch* is the pixel size at the sensor and is 16x8 μm. This 2x1 ratio size means the camera gathers two spectral pixels for each spatial pixel. The ratio between spectral and spatial pixels can be changed (i.e., 4x1 or 8x1), but the spatial dimension of a detector's pixel does not vary and is 8 μm. Regardless, the pixel size at the scene plane, called *pixel size*, is not 8 μm. It depends on the FOV, the number of effective strip pixels, and the focusing distance from the lens. The third may vary if the first two parameters are determined (38 ° and 1024 pixels). In this manuscript, we decided to operate constantly at a focusing distance of 15 cm. Hence, it was possible to calculate the size of a pixel at the scene plane with the following formula:

$$Pixel\ size = \tan\left(\frac{FOV}{2}\right) \cdot \frac{2h}{N_p} \quad (1)$$

In the above equation,  $h$  is the object's distance from the target,  $FOV$  is the angle described earlier, and  $N_p$  is the number of strip pixels. Hence, employing our datasheet's values, the outcome is approximately 100 μm. The total imaged scene's width, also known as *field dimension*, depends on the following trigonometric formula:

$$Field\ dimension = 2h \cdot \tan\left(\frac{FOV}{2}\right) \quad (2)$$

It corresponds to the *pixel size* multiplied by  $N_p$  (i.e., 1024), which is approximately 10.3 cm. Figure 3 exhibits the computations just mentioned above.

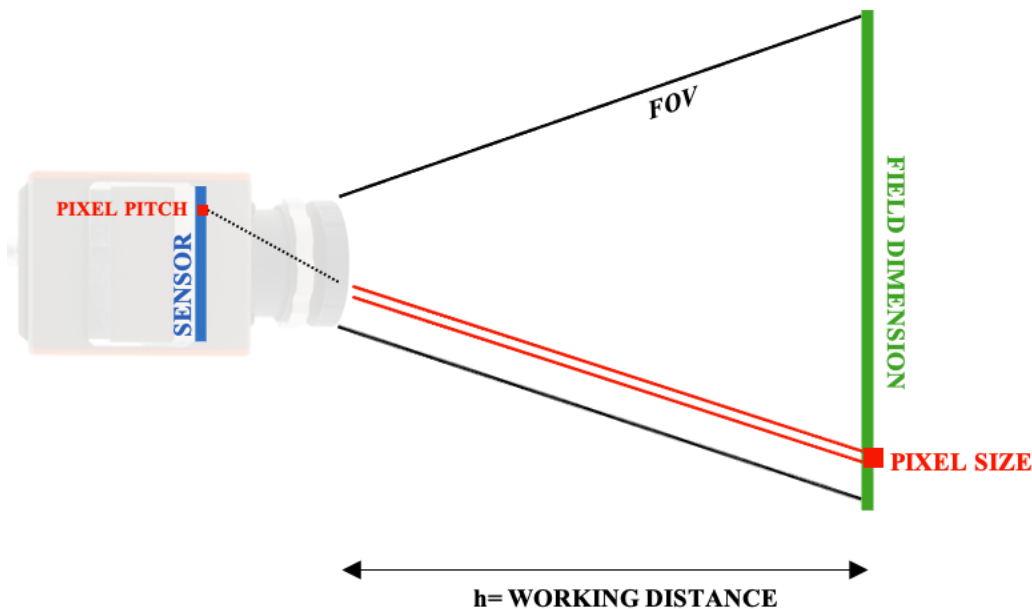


Figure 3 - Hyperspectral camera optical schema for trigonometric equations

The evaluations concerning the FX10e's optical characteristics are meaningful in design and functional importance, as we will see in the following paragraphs, concerning the camera's frame rate and motor's movement synchronization.

## 2.2 The motion system

The motion system comprises a recirculating linear ball screw guide, a stepper motor and a driver controlled by an Arduino Uno board. This system can collect line by line the reflectance spectrum of any region of interest<sup>11,15,18</sup>. Pushbroom cameras require a linear movement between the camera and the sample to allow complete scanning, either by moving the camera or the sample at a controlled and constant speed. Concerning a skin cancer application, we designed a system where the camera moves while the target is stationary. Thus, the synchronization between movement and acquisition is fundamental. Appropriate calculations concerning the previous section and the design of a software interface controlling the motor's motion enable such synchronization.



Figure 4 - Recirculating ball screw drive

The linear ball screw guide is made of aluminum and has a length of 200 mm, a diameter of 12 mm and a pitch of 4 mm (Figure 4). The screw guides the Schneider Electric NEMA 17 stepper motor's shaft. If  $N$  is the number of motor expansions at each step, the motor moves by  $\theta = 360^\circ / 4N$ , controlling the angular position and speed by varying the steps' frequency. NEMA17 performs  $1.8^\circ$  of angular displacement at each step, taking 200 steps to complete a revolution. It is driven in current by a TB6600 Driver (Figure 5), which controls its speed and direction.



Figure 5 - Microstep-based motor driver

The driver allows selecting between eight *micro-steps* (Figure 6), enabling the motor's angular step division into n sub-steps. Thirty-two micro-steps (Figure 6) resemble a 0.05625° step angle, resulting in 6400 steps for a complete revolution. The *pitch* of the screw corresponds to its linear motion and equals 4 mm. Hence, in our configuration, the motor makes 0.625 μm at each micro-step. Also, the driver supplies 1.5 A to the motor, as the datasheet suggests.

Micro Step	Pulse/Rev	S1	S2	S3
NC	NC	ON	ON	ON
1	200	ON	ON	OFF
2/A	400	ON	OFF	ON
2/B	400	OFF	ON	ON
4	800	ON	OFF	OFF
8	1600	OFF	ON	OFF
16	3200	OFF	OFF	ON
32	6400	OFF	OFF	OFF

Figure 6 - Motor driver's datasheet

An Arduino Uno board controls then the driver. We programmed the board through the Arduino IDE (Integrated Development Environment), where the *sketches* are written in *Wiring*, similar to the C language, allowing flashing to the board.

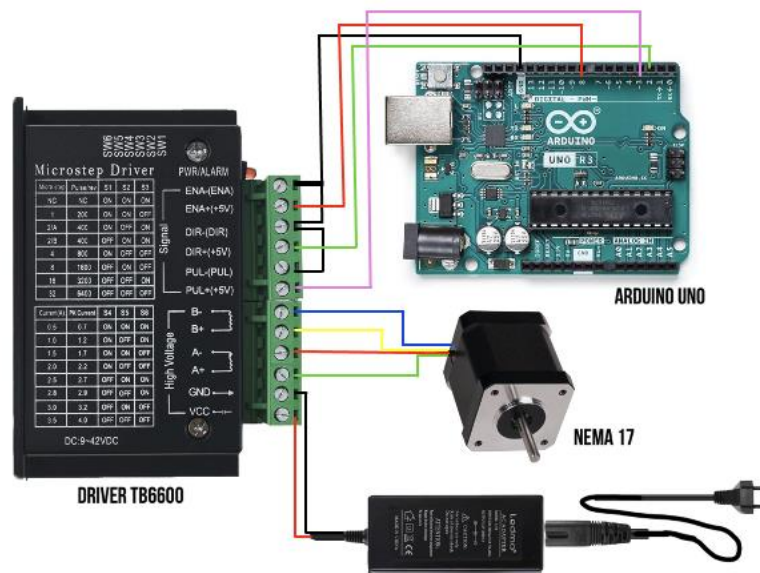


Figure 7 - Electrical configuration of the hyperspectral blueprint

Figure 7 displays the wiring diagram of the motor, driver and board connections. We suitably positioned the power supply, driver, and board and fixed them inside a single container for electrical components measuring 190x140x70 mm, placed near the linear guide.

### 2.3 The illumination system

In a hyperspectral imaging system, the scene's illumination is fundamental. Indeed, any camera measures the light beam reflected by the object of interest. In hyperspectral application, researchers must carefully choose the light source according to its sensitive wavelengths. Proper illumination is characterised by a continuous intensity spectrum, without peaks and with a good intensity contribution in amplitude<sup>11,16,17</sup>.

Natural scene illumination, i.e. sunlight, is an excellent option for continuity and intensity spectrum at all wavelengths. Nonetheless, it is not easy to handle as it varies rapidly in direction, intensity and colour. On the other hand, an artificial light source has the advantage of allowing complete control in terms of direction, intensity, and scattering and provides repeatability in acquisition conditions.

In our case, we sought illumination with a continuous spectrum and good intensity in the range between 400 and 1000 nm, in which the Specim FX10e camera used in this acquisition system operates. To choose between the different light source options, we directed the light source towards the white reference and visualised the reflectance using Specim LUMO.

Hence, the illumination system operated in this work is the THORLABS OSL2BIR 150 W 3200 K, which has an aluminum-coated reflector for improved infrared performance, and the specifications include the intensity spectrum shown in Figure 8. The illumination system comprises two bulbs mounted on two supports which we arranged to be directed to the region of interest and granting distance regulation.

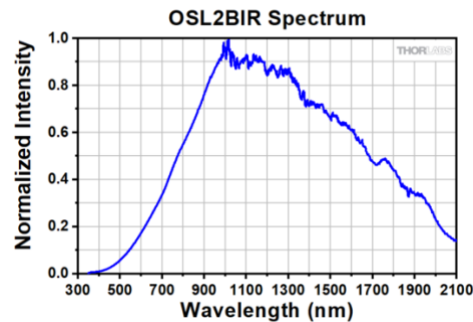


Figure 8 - THORLABS OSL2BIR 150 W 3200 K intensity spectrum

### 2.4 Image calibration

Several steps must be taken to obtain a hyperspectral datacube with a pushbroom camera correctly. We mentioned how optical variables, the motion system, the need for synchronisation, and correct illumination influence the data quality. Another crucial step is the image calibration process<sup>12,14,19</sup>. For each pixel, the hyperspectral camera sensor measures the reflected energy onto the frames constituting the hypercube, each pixel having a digital value. However, the sensor's response is not uniform over the covered spectral range. The consequence is that even if the same amount of radiation hits each sensor pixel equally, the measured digital value might differ. In addition, illumination conditions may not be uniform over the covered spectral range.

The calibration methodology overcomes the challenges mentioned above, and the following equation determines it:

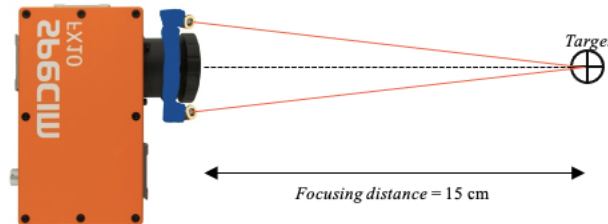
$$\text{reflectance} = \frac{\text{raw image} - \text{black reference}}{\text{white reference} - \text{black reference}} \quad (3)$$

In the equation, the white reference is the image of a zenith polymer white calibration panel that is certified to reflect more than 95 per cent of the incident radiation in the range of 400 to 2500 nm<sup>17</sup>. We placed the white reference panel at 15 cm. The dark reference, on the other hand, represents the minimum value that the sensor measures when no radiation hits it. We ultimately closed the camera length to obtain the black reference.

## 2.5 Target centering and distancing

We faced two practical problems in obtaining images: correct focusing distance measuring and target centring. We devised a system based on small laser diodes to overcome these problems. We attached on a custom-made 3D-printed crown (Figure 9) two 5 mW - 5 V small red laser emitting diodes, both driven by the Arduino board.

Figure 9 - 3D-printed crown and red-emitting diodes housing



The emitters meet at a precise distance of 15 cm, the focusing distance, at the centre of the lens. The diodes are only switched on in the moments immediately prior to the acquisition, we check the distancing and centring, and then the scanning process can begin.

## 2.6 Camera control, system synchronisation and image scanning

The Specim FX10e camera's rear panel has two connectors: the 12 V DC power cable and a GigE connector. The GigE Vision protocol is a global interface standard for video transfer designed for high-performance industrial cameras and for controlling devices over Ethernet networks. Hence, we designed a system to acquire images in the laboratory using any Generic Interface for Cameras (GenICam) compliant hyperspectral camera using the gigabit ethernet interface<sup>17</sup>. The camera gathers and sends information via ethernet when a trigger arrives, allowing the camera's image sensor exposure to start. It can be generated internally by the camera (free running) or by an external device (external trigger). In this blueprint, we adopted the external triggering mode to synchronise the motor's motion and camera frame rate.

We operated the python *pyserial* library to control the motor, facilitating software communication with the Arduino's serial port. Accurate speed and position control of the motor are essential to obtain a correct hypercube acquisition. Since the scanning result is closely related to the concepts of trigger and exposure time, the accuracy and smoothness of the camera movement directly influence it<sup>17</sup>.

Along with *pyserial*, we operated the *harvester* library, which guarantees image acquisitions under the GenICam (Generic Interface for Cameras) standard<sup>17</sup>. Through the Harvester routines, it is possible to perform the main camera control actions, such as starting and stopping the data flow, gathering the captured frames and storing them to disk, and configuring any acquisition-related parameter. The combination of the functionalities provided by the *harvester* and *pyserial* libraries makes it possible to control the camera and motor simultaneously, offering the opportunity to synchronise them. We met motion-acquisition synchronisation by adjusting the control signals accordingly. The PWM signal generated by the Arduino board's pin regulates the movement, controlling the motor's steps. With each signal's positive edge, the motor takes one step. We can control the motor's direction by operating another board's pin. Hence the need to capture frames via external triggering. The camera performs a frame capture at each positive edge of the trigger signal, driven by the *harvester* library.

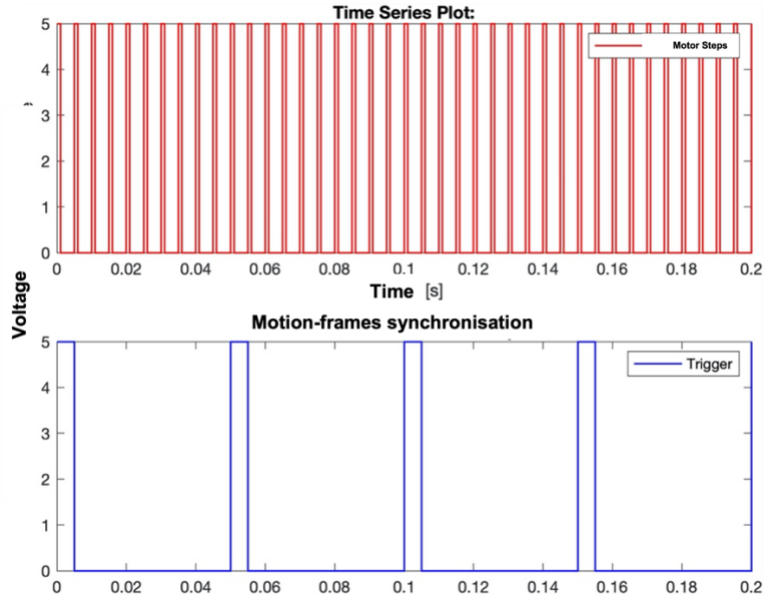


Figure 10 - Motion-frames synchronisation

Concerning the optical evaluations carried out in Section 2.1, we should notice that the pixel size at the image level is approximately  $100\ \mu\text{m}$ . Therefore, we must sample at least once every  $100\ \mu\text{m}$  linear displacement to obtain a complete image. The motor performs  $2.5\ \mu\text{m}$  of linear displacement at each step in our configuration. Hence, 40 motor steps are required to perform  $100\ \mu\text{m}$ . We captured four frames every  $100\ \mu\text{m}$  and averaged them to avoid aliasing and noise (Figure 10). Hence, the Arduino Uno board sends a pulse to the motor every ten steps and a pulse to the trigger pin simultaneously as the tenth motor pulse. This way, a scene frame is captured every ten motor steps. This configuration synchronises the signals and guarantees precise and fully controlled capturing.

The choice of motor step was made to optimise acquisition quality and time. In this mode, to acquire an area of  $10 \times 2\ \text{cm}$ , the acquisition time is 40 seconds.

## 2.7 The Graphical User Interface

We designed the GUI using the PyQt5 python library (Figure 11). The development uses a drag-and-drop process which facilitates the interface creation process. It is necessary to define the main window, divide it into frames, assign types and names to the different elements and position the buttons as desired. At the end of this step, the library generates the corresponding code in Python, which can also be modified. The various generated buttons can be assigned and linked to any custom routine. The interface considerably improves the system's usability, makes the button-action relationship performed immediately and facilitates the acquisition process<sup>17</sup>.

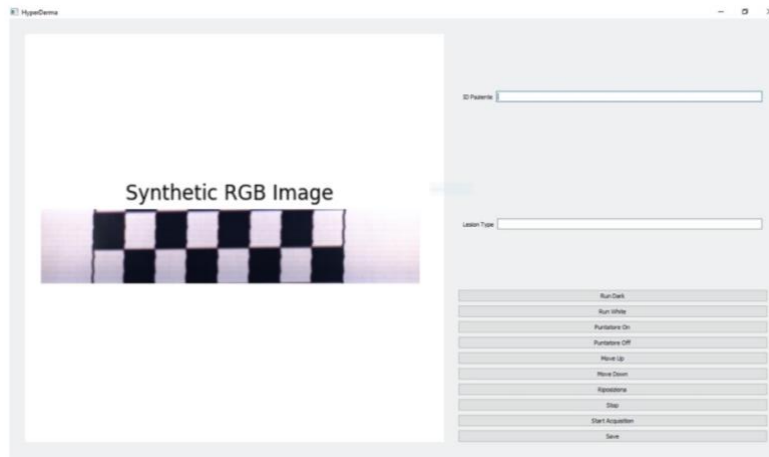


Figure 11 - Graphical User Interface (GUI) designed for the blueprint

The GUI (Graphical User Interface) implemented, as shown in Figure 11, includes the following command buttons and text fields:

- Patient ID: this text field must be filled in to store the files referring to the acquisition performed with this identifier
- Lesion Type: the acquired file is also assigned a preliminary classification based on the doctor's belief
- Run Dark: the calibration of the black reference performs an image acquisition with the lens closed and stores a *numpy* file with which the system can perform the calibration later
- Run White: the white reference calibration performs an image acquisition upon the white reference panel placed in front of the camera at 15 cm, and stores a *numpy* file with which the system can perform the calibration later.
- Pointer On: turns on the laser diodes, to be used just before acquisition to centre the target
- Pointer Off: turns off the laser pointer diodes
- Move Up: moves the camera up and continues to move up until the button *Stop* is pressed
- Move Down: Moves the camera downwards, and continues to move down until the button *Stop* is pressed
- Stop: Stops the motor
- Start Acquisition: it starts the scanning process. The camera moves up 1 cm and then down 2 cm, capturing the scene's frames
- Save: stores a series of files referring to the datacube *.npy*, *.img*, *.hdr* and the RGB image in *.png* format

At the end of an acquisition process, namely approximately 40 seconds after clicking on the Start Acquisition command, a synthetic RGB image (synthesised from three bands: Red = 700.47 nm, Green = 546.09 nm and Blue = 435.79 nm, calculated within the 224 bands acquired between 400 nm and 1000 nm) of the captured scene can be displayed on the left panel in Figure 11 to verify the success of the operation immediately. If the Patient ID and Lesion Type text fields are not filled in, a popup will remind it and ensure the data is saved correctly.

### 3. VALIDATION

We considered some crucial metrics to guarantee the system's repeatability. Hence, the main objective of this analysis is to assess the system's ability to acquire the same scene under comparable conditions with similar results. This procedure ensures that the tool is not heavily dependent on uncontrolled variables and that the information faithfully represents the scene's characteristics at the time of capture. We gathered images by repeating the capture procedure under the same lighting conditions. To be sure of acquiring the same spatial window, the procedure employed the reposition command,

which is present within the GUI (Figure 11). When performing a traditional acquisition, once centred on the target, the system moves up 1 cm and then down by capturing 2 cm frames. In this way, ten images of the same target object were collected through repeated consecutive acquisitions, and from these were extrapolated specific indices and comparison graphs.

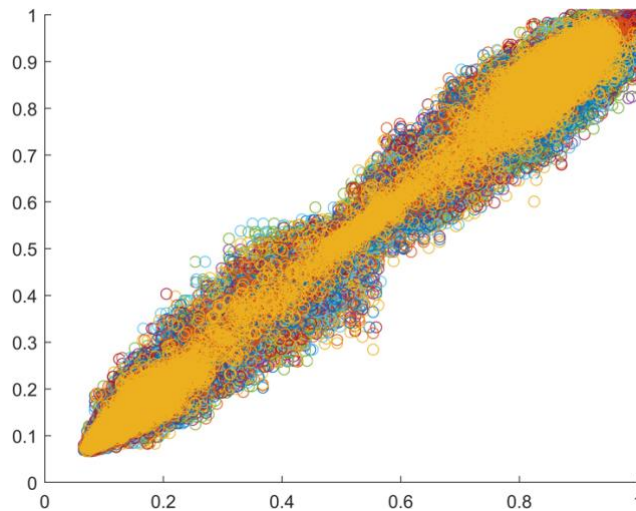


Figure 12 - Voxel values to analyse repeatability

The first graph displays the differences between these images in a scatter plot, in which all the volumetric picture element (i.e., voxels) values of each of the two hyperspectral images compared are shown on the two axes. The voxel value represents the reflectance of light in each pixel of the hyperspectral image at a given wavelength<sup>16</sup>. A scatter plot can be an effective tool to visualise the degree of correlation between the two variables placed on the axes. Ideally, the scatter plot should be a bisector line between the positive half-axis of the abscissas and the positive half-axis of the ordinates, which would indicate that each corresponding voxel pair between the two images contains the same information. The comparisons for all possible image combinations resulted in Figure 12's plot. The tendency of the points of the scatter plot, which identify the values assumed by the corresponding voxels of the two different images, along the bisector testifies to the high degree of correlation between two successive acquisitions and is, therefore, an index of repeatability<sup>16</sup>.

Another index that has been extrapolated from the successive acquisitions is the Relative Percentage Difference (RPD), calculated as shown in the equation below:

$$RPD (\%) = 200 \cdot \frac{|R1 - R2|}{R1 + R2} \quad (4)$$

R1 and R2 correspond to the compared HSIs and measure the percentage of how much one differs from the other. Lower values of RPD represent more significant similarity. In our case, we compared all possible combinations and derived the average value. The calculated average RPD is 12.45%, again giving us a remarkable degree of repeatability<sup>17</sup>.

The last measure considered is the Structural Similarity Index Method (SSIM). It is a well-known quality metric used to measure the similarity between two images and is related to the quality perception of the human visual system (HVS). Instead of traditional error summation methods, SSIM models any image distortion as a combination of correlation loss, luminance distortion and contrast distortion<sup>17</sup>. The similarity index has a decimal value between 0 and 1; value 1 indicates two identical images, and value 0 indicates no similarity. An average SSIM of 0.8725 was derived.

#### 4. CONCLUSIONS

Here, we presented a hyperspectral acquisition system engineered to gather diagnostic clinical data concerning skin cancer. It is enhanced by a linear synchronous motion, an appropriate illumination system, a 3D-printed circular crown containing targeting and distancing emitting diodes, and software modules supported by open-source packages. The hyperspectral system enables image collection with any hyperspectral pushbroom camera following the GigE vision interface standard.

Furthermore, we validated the architecture to check synchronisation between motor and camera frame rate, calibration, and the scene's capturing repeatability. In the future, we aim to collect an online database of clinical hyperspectral images.

In conclusion, the main contribution of our work is to serve as a guide for any research group working on hyperspectral technologies. We presented all the information to accurately capture spectral information and techniques to validate the correct operation of the system. First, the whole system works with any GenICam protocol-compliant camera. Secondly, we operated cheap and promptly available hardware and open-source software to enable research groups to work with hyperspectral systems most efficiently. Indeed, all software modules used in this development are open source, allowing high flexibility and representing a lower-cost approach compared to market solutions.

## REFERENCES

- [1] Ferlay, J., Colombet, M., Soerjomataram, I., Parkin, D. M., Piñeros, M., Znaor, A. and Bray, F., "Cancer statistics for the year 2020: An overview," *Int J Cancer* **149**(4), 778–789 (2021).
- [2] Scolyer, R. A., Long, G. v. and Thompson, J. F., "Evolving concepts in melanoma classification and their relevance to multidisciplinary melanoma patient care," *Mol Oncol* **5**(2), 124–136 (2011).
- [3] Siegel, R. L., Miller, K. D., Fuchs, H. E. and Jemal, A., "Cancer statistics, 2022," *CA Cancer J Clin* **72**(1), 7–33 (2022).
- [4] Ciężyńska, M., Kamińska-Winciorek, G., Lange, D., Lewandowski, B., Reich, A., Sławińska, M., Pabianek, M., Szczepaniak, K., Hankiewicz, A., Ułańska, M., Morawiec, J., Błasińska-Morawiec, M., Morawiec, Z., Piekarski, J., Nejc, D., Brodowski, R., Zaryczańska, A., Sobjanek, M., Nowicki, R. J., et al., "The incidence and clinical analysis of non-melanoma skin cancer," *Scientific Reports* 2021 11:1 **11**(1), 1–10 (2021).
- [5] Dildar, M., Akram, S., Irfan, M., Khan, H. U., Ramzan, M., Mahmood, A. R., Alsaiari, S. A., Saeed, A. H. M., Alraddadi, M. O. and Mahnashi, M. H., "Skin Cancer Detection: A Review Using Deep Learning Techniques," *International Journal of Environmental Research and Public Health* 2021, Vol. 18, Page 5479 **18**(10), 5479 (2021).
- [6] Haggemüller, S., Maron, R. C., Hekler, A., Utikal, J. S., Barata, C., Barnhill, R. L., Beltraminelli, H., Berking, C., Betz-Stablein, B., Blum, A., Braun, S. A., Carr, R., Combalia, M., Fernandez-Figueras, M. T., Ferrara, G., Freitag, S., French, L. E., Gellrich, F. F., Ghoreschi, K., et al., "Skin cancer classification via convolutional neural networks: systematic review of studies involving human experts," *Eur J Cancer* **156**, 202–216 (2021).
- [7] Rey-Barroso, L., Peña-Gutiérrez, S., Yáñez, C., Burgos-Fernández, F. J., Vilaseca, M. and Royo, S., "Optical Technologies for the Improvement of Skin Cancer Diagnosis: A Review," *Sensors* 2021, Vol. 21, Page 252 **21**(1), 252 (2021).
- [8] Jiang, S., Li, H. and Jin, Z., "A Visually Interpretable Deep Learning Framework for Histopathological Image-Based Skin Cancer Diagnosis," *IEEE J Biomed Health Inform* **25**(5), 1483–1494 (2021).
- [9] Goyal, M., Knackstedt, T., Yan, S. and Hassanpour, S., "Artificial intelligence-based image classification methods for diagnosis of skin cancer: Challenges and opportunities," *Comput Biol Med* **127**, 104065 (2020).
- [10] Yu, K. H., Beam, A. L. and Kohane, I. S., "Artificial intelligence in healthcare," *Nature Biomedical Engineering* 2018 2:10 **2**(10), 719–731 (2018).
- [11] Lu, G. and Fei, B., "Medical hyperspectral imaging: a review," <https://doi.org/10.1117/1.JBO.19.1.010901> **19**(1), 010901 (2014).

- [12] Torti, E., Leon, R., Salvia, M. la, Florimbi, G., Martinez-Vega, B., Fabelo, H., Ortega, S., Callicó, G. M. and Loporati, F., “Parallel Classification Pipelines for Skin Cancer Detection Exploiting Hyperspectral Imaging on Hybrid Systems,” *Electronics* 2020, Vol. 9, Page 1503 **9**(9), 1503 (2020).
- [13] Khan, U., Paheding, S., Elkin, C. P. and Devabhaktuni, V. K., “Trends in Deep Learning for Medical Hyperspectral Image Analysis,” *IEEE Access* **9**, 79534–79548 (2021).
- [14] Florimbi, G., Fabelo, H., Torti, E., Ortega, S., Marrero-Martin, M., Callico, G. M., Danese, G. and Loporati, F., “Towards Real-Time Computing of Intraoperative Hyperspectral Imaging for Brain Cancer Detection Using Multi-GPU Platforms,” *IEEE Access* **8**, 8485–8501 (2020).
- [15] Li, Q., He, X., Wang, Y., Liu, H., Xu, D. and Guo, F., “Review of spectral imaging technology in biomedical engineering: achievements and challenges,” <https://doi.org/10.1117/1.JBO.18.10.100901> **18**(10), 100901 (2013).
- [16] Leon, R., Martinez-Vega, B., Fabelo, H., Ortega, S., Melian, V., Castaño, I., Carretero, G., Almeida, P., Garcia, A., Quevedo, E., Hernandez, J. A., Clavo, B. and Callico, G. M., “Non-Invasive Skin Cancer Diagnosis Using Hyperspectral Imaging for In-Situ Clinical Support,” *Journal of Clinical Medicine* 2020, Vol. 9, Page 1662 **9**(6), 1662 (2020).
- [17] Morales, A., Horstrand, P., Guerra, R., Leon, R., Ortega, S., Díaz, M., Melián, J. M., López, S., López, J. F., Callico, G. M., Martel, E. and Sarmiento, R., “Laboratory Hyperspectral Image Acquisition System Setup and Validation,” *Sensors* 2022, Vol. 22, Page 2159 **22**(6), 2159 (2022).
- [18] Khan, U., Paheding, S., Elkin, C. P. and Devabhaktuni, V. K., “Trends in Deep Learning for Medical Hyperspectral Image Analysis,” *IEEE Access* **9**, 79534–79548 (2021).
- [19] la Salvia, M., Torti, E., Leon, R., Fabelo, H., Ortega, S., Balea-Fernandez, F., Martinez-Vega, B., Castaño, I., Almeida, P., Carretero, G., Hernandez, J. A., Callico, G. M. and Loporati, F., “Neural Networks-Based On-Site Dermatologic Diagnosis through Hyperspectral Epidermal Images,” *Sensors* **22**(19), 7139 (2022).